

Experimental and numerical study of electrically-driven MHD flow in a modified cylindrical annulus: (2) Instabilities

Zacharias Stelzer,¹ Sophie Miralles,¹ David Cébron,^{1,2} Jérôme Noir,¹ Stijn Vantieghem,¹ and Andrew Jackson¹

¹*Institute of Geophysics, ETH Zürich, Switzerland*

²*Université Grenoble Alpes, CNRS, ISTERRE, Grenoble, France*

(Dated: June 26, 2015)

We present an investigation of the stability of liquid metal flow under the influence of an imposed magnetic field by means of a laboratory experiment as well as a linear stability analysis of the setup using the finite element method. The experimental device ZUCCHINI is a modified cylindrical annulus with electrically-driven flow of liquid GaInSn operating at Hartmann and Reynolds numbers up to $M = 2022$ and $Re = 2.6 \cdot 10^5$ respectively. The magnetic field gives rise to a free shear layer at the prominent inner electrode.

We identify several flow regimes characterized by the nature of the instabilities. Above a critical current $I_c = \mathcal{O}(0.1 \text{ A})$, the steady flow is destabilized by a Kelvin-Helmholtz mechanism at the free shear layer. The instability consists of counterrotating vortices traveling with the mean flow. For low forcing, the vortices are restricted to the free shear layer. Their azimuthal wave number m grows with M and decreases with Re . At $Re/M \approx 25$, the instability becomes container-filling and energetically significant. It enhances the radial momentum transport which manifests itself in a broadening of the free shear layer width δ_S . We propose that this transition may be related to an unstable Hartmann layer. At $Re/M^2 = \mathcal{O}(1)$, an abrupt change is observed in the mean azimuthal velocity $\langle \overline{u_\phi} \rangle$ and the friction factor F , which we interpret as the transition between an inertialess and an inertial regime.

I. INTRODUCTION

In the context of geo- and astrophysics as well as engineering applications, it is of great interest to study the interaction between electrically conducting fluids and magnetic fields. This research area is called magneto-hydrodynamics (MHD). Two MHD regimes can be distinguished by the value of the magnetic Reynolds number $Rm = \mu_0 \sigma_e U_0 a$ where μ_0 is the permeability of free space, σ_e the electrical conductivity, U_0 a typical velocity and a the length scale of the system. On the one hand is the regime of large Rm where e.g. planetary dynamos live [1]. It is characterized by a two-way interaction between flow and magnetic field. On the other hand is the regime of small $Rm \lesssim 1$ and small Lundquist number $S = (\mu_0/\rho)^{1/2} \sigma_e a B_0 \lesssim 1$ with ρ the mass density and B_0 the strength of the imposed magnetic field. This regime is characterized by the absence of the reaction of the flow on the magnetic field which means that induced fields are negligible. Many liquid-metal experiments and engineering applications fall into this so-called quasi-static limit [2]; it is also believed to govern the small-scale motions in the Earth's core [3].

The experiment ZUCCHINI (ZURich Cylindrical CHANNEL INstability Investigation) allows us to study electrically-driven MHD flow at low Rm in the modified cylindrical annulus shown in Figure 1. All side walls are electrically insulating except the inner and outer ring electrodes. Forcing a radial electrical current I through the tank filled with liquid GaInSn under an imposed magnetic field \mathbf{B} gives rise to a Lorentz force leading to a mainly azimuthal flow. The system is controlled by two nondimensional parameters, namely the Hartmann num-

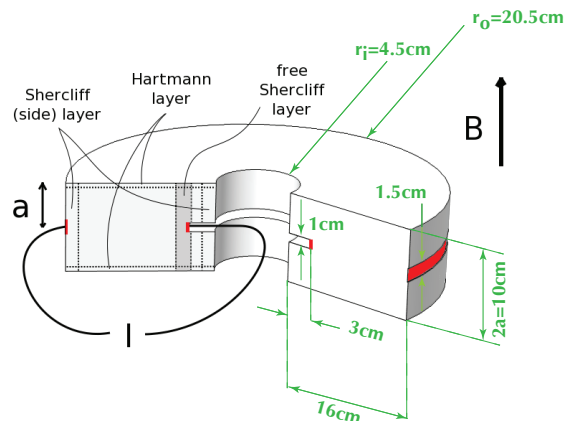


FIG. 1. Sketch of the modified cylindrical annulus ZUCCHINI with dimensions. Forcing an axisymmetric electrical current I through the liquid metal under an imposed magnetic field \mathbf{B} gives rise to a Lorentz force which drives an azimuthal flow. The electrodes are coloured in red, the remaining walls are insulating. The half-height $a = 5 \text{ cm}$ is used as length scale in the non-dimensionalization.

ber M and the Reynolds number Re ,

$$M = aB_0 \sqrt{\frac{\sigma_e}{\rho\nu}}, \quad Re = \frac{U_0 a}{\nu}. \quad (1)$$

where ν is the kinematic viscosity of the fluid.

In the first part of this work [4], hereafter referred to as ‘Paper 1’, we investigated the steady base flow experimentally as well as numerically. Also a detailed description of the setup and previous experiments is found there. In the current study, we focus on the instabilities of the

flow which will be shown to originate from the free shear layer near the inner electrode.

Most earlier experiments in similar geometries operated in the unstable regime and used global potential difference measurements to diagnose the flow [5–7]. Transitions in flow regimes were diagnosed by the friction factor F , defined in Equation 18 or similar quantities describing the dissipation in the system. Some experiments probed the flow structure locally by potential difference probes (PDP) [8, 9] or ultrasonic Doppler velocimetry (UDV) [10]. We employ both local and global measurements.

The most significant difference between ZUCCHINI and most other experiments is the presence of the inner electrode which protrudes into the flow. Since the magnetic field suppresses gradients along its direction, a free shear layer develops at the edge of the electrode. In addition the Hartmann layers at walls perpendicular to the field with thickness $\delta_H \sim M^{-1}$ and Shercliff (side) layers at parallel walls scaling as $\delta_S \sim M^{-1/2}$ are important features of confined low- Rm MHD flow.

Experimental investigations naturally incorporate the whole physics of a system. Due to the sparsity of experimental measurements, it is instructive to complement the experiment by numerical simulations which, however, do not reach the same parameter values. The famous Moresco and Alboussière [7] experiment (MA04) studying the instability of the Hartmann layer as well as the original Hartmann and Lazarus [11] duct experiment have been the topic of intense numerical investigations. Krasnov *et al.* [12] explained the discrepancy in the value for the threshold of instability between results of MA04 ($Re_c/M \approx 380$) and the linear stability analysis which is two orders of magnitude larger by finite-amplitude perturbations. Vantieghem and Knaepen [13] found that the magnetic field suppresses turbulence in the core and the Hartmann layers and that unstable side layers can coexist with stable Hartmann layers. Zhao and Zikanov [14] studied the MA04 setup below the threshold of Hartmann layer instability for a Hartmann number of $M = 260$. They found that a first instability limited to the outer side layer does not change the friction factor F much which is dominated by stresses at the Hartmann walls. This picture of subsequent relaminarization of the core flow, the Hartmann layers and finally the side layers with increasing magnetic field was confirmed by the straight duct simulations of Krasnov *et al.* [15] at $Re = 10^5$ and $M \in [0, 400]$. Not only the critical parameters for the laminar-turbulent transition but also friction coefficients were in agreement with Hartmann’s original data [16].

Another approach for the numerical simulation of MHD flow at large Hartmann numbers M and interaction parameters $N = M^2/Re$ is the effective two-dimensional model of Pothérat *et al.* [17, 18]. It is based on the assumption of a quasi-2D core flow, and includes 3D effects due to the Hartmann layers in the averaged equations. It has been validated against experimental results, e.g. the free shear layer study of Alboussière *et al.* [8]. A similar concept underlies the geostrophic-like model by

Alboussière [19, 20] for large- M flows.

Free MHD shear layers have been studied theoretically [21, 22], experimentally [8, 9, 23, 24] and numerically [18, 24]. Lieutaud and Neel [22] studied the stability of electrically-driven shear flow in a straight duct against two-dimensional perturbations, and found the limit of unconditional stability below which any arbitrary 2D perturbation decays. The MATUR experiment examined the structure as well as momentum transport of a quasi-2D MHD turbulent shear layer at $M = 42$ and up to 1800 in [7, 8], respectively. It was found that the shear layer thickness is significantly increased and scales as $\delta_S \sim (M/Re)^{-1/2.3}$, the laminar prediction being $\delta_S \sim M^{-1/2}$. The velocity field is dominated by a small number of large coherent structures moving with a transit velocity of slightly above $u_{\phi,max}$. In the Princeton MRI experiment [23, 24], a free Shercliff layer was studied in the presence of rotation and magnetic field in a cylindrical Taylor-Couette apparatus. Finally the Taylor-Couette experiment DTS observed magneto-inertial waves in spherical geometry [25, 26].

The present paper focuses on the instabilities in ZUCCHINI. Section II summarizes the physical model which can be found in more detail in Paper 1, as well as the numerical and experimental methods. Section III describes our findings for the mean flow, the instability of the free shear layer and further transitions in the friction factor. A discussion in Section IV concludes the work.

II. MODEL AND METHODS

The configuration is a cylindrical annulus filled with an electrically conducting fluid. The basic setup is shown in Figure 1. The half-height of the container is $a = 5$ cm. The radii of the inner and outer cylinders are $r_i = 4.5$ cm and $r_o = 20.5$ cm, respectively. The disk electrode protruding from the inner cylinder has a radius of $r_d = 7.5$ cm, its axial width is 1 cm. Container and fluid are subject to an imposed axial magnetic field $\mathbf{B} = B_0 \mathbf{e}_z$ with a strength of up to 1 T. We force an electrical current I of up to 300 A between the edge of the disk electrode at the center and the ring electrode at the outer cylinder. The remaining walls of the container are electrically insulating. The mainly radial current density \mathbf{j} in an axial magnetic field gives rise to a Lorentz force $\mathbf{f}_L = \mathbf{j} \times \mathbf{B}$ in the azimuthal direction resulting in an azimuthal fluid flow.

With $Rm \lesssim \mathcal{O}(10^{-1})$ as an indicator of the ratio of induced to imposed magnetic fields, induced fields are largely negligible in ZUCCHINI. For this so-called quasi-static approximation ($Rm \ll 1$), the dimensional governing equations are the Navier-Stokes equation, the incompressible continuity equation, Ohm’s law and the equa-

tion of charge conservation,

$$\rho \left(\frac{\partial \mathbf{u}}{\partial t} + \mathbf{u} \cdot \nabla \mathbf{u} \right) = -\nabla p + \rho \nu \nabla^2 \mathbf{u} + \mathbf{j} \times \mathbf{B} \quad (2)$$

$$\nabla \cdot \mathbf{u} = 0 \quad (3)$$

$$\mathbf{j} = \sigma_e (\mathbf{E} + \mathbf{u} \times \mathbf{B}) \quad (4)$$

$$\nabla \cdot \mathbf{j} = 0, \quad (5)$$

where \mathbf{u} is the velocity vector, \mathbf{E} is the electric field and p is the pressure. The nondimensional equations are

$$\frac{Re}{M^2} \left(\frac{\partial \mathbf{u}}{\partial t} + \mathbf{u} \cdot \nabla \mathbf{u} \right) = -\nabla p + \frac{1}{M^2} \nabla^2 \mathbf{u} + (-\nabla \Phi + \mathbf{u} \times \mathbf{B}) \times \mathbf{B} \quad (6)$$

$$\nabla \cdot \mathbf{u} = 0 \quad (7)$$

$$\nabla^2 \Phi = \nabla \cdot (\mathbf{u} \times \mathbf{B}) \quad (8)$$

as derived in Paper 1. The nondimensional parameters governing the system are the Hartmann number M and the Reynolds number Re defined in Equation 1. The square of the Hartmann number M^2 gives the ratio of Lorentz to viscous forces. The Reynolds number Re is the ratio of inertial to viscous forces. Alternatively the interaction parameter $N = M^2/Re$ can be used which gives the ratio of Lorentz to inertial forces.

A. Numerical simulation

We assume that the base flow in ZUCCHINI is steady and axisymmetric as established in Paper 1. In reality, such a flow occurs only at very low forcing. For a given Hartmann number M , the flow may be unstable to infinitesimally small perturbations in the velocity field above a critical value Re_c of the Reynolds number, called the linear onset of instability. These perturbations initially grow like $e^{\sigma t}$ where σ is the growth rate. The flow could also be unstable to finite-amplitude perturbations potentially already below the linear onset of instability, $Re < Re_c$, called a subcritical instability. With the linear instability analysis, we hence find an upper bound for the onset of instability.

As for the base flow, we perform numerical simulations using the commercial finite element (FE) code Comsol Multiphysics, version 4.3b. The brute force approach of recovering the unstable flow by 3D simulations is too costly since very thin boundary layers $\delta_H \sim M^{-1}$ have to be resolved. Hence we choose to study the linear onset of instability by simulating modes with different azimuthal wave numbers m separately. The separation is possible since modes with different m are not coupled in the linear problem. In this way, the problem reduces to 2D3C (2 dimensions, 3 components) simulations.

1. First-order perturbation equations

For the study of the linear onset of instability, the velocity field is expressed as a sum of the steady and axisymmetric base flow \mathbf{u}^b and a harmonic perturbation \mathbf{u}' with an explicit ϕ -dependence using the azimuthal wave number m ,

$$\mathbf{u} = \mathbf{u}^b(r, z) + \mathbf{u}'(r, z, t) e^{im\phi}. \quad (9)$$

The perturbation is assumed to be small compared to the base flow, $|\mathbf{u}'| = \epsilon |\mathbf{u}^b|$ with $\epsilon \ll 1$. The same procedure is applied to the remaining variables pressure p and the electric potential Φ . Inserting these expressions into the governing Equations 6-8 yields terms of order ϵ^0 , ϵ^1 and ϵ^2 . Terms of order zero that constitute the base flow (equivalent to Eq. 6-8) were solved in Paper 1, second-order terms are negligible. The remaining terms of order one in ϵ make up the linearized perturbation equations. They are given in cylindrical coordinates in Appendix A.

2. Numerical model

The linearized perturbation equations (Eq. A1-A5) as well as the equations for the axisymmetric base flow (Eq. 6-8) are solved with the FE method. The 2D geometry corresponds to a (r, z) -plane section through the experimental setup of ZUCCHINI. Details of the implementation are found in Paper 1. In the present study, we use quadratic and linear Lagrange elements for the discretization of velocity and pressure fields, respectively; the discretization of the electric potential is quadratic. In order to further reduce computation time, the mesh is adapted for every M . The differences in global and local measurements of velocity and electrical current density compared with highly resolved simulations from Paper 1 are negligible ($\lesssim 0.1\%$).

Velocity boundary conditions are no slip, $\mathbf{u} = \mathbf{0}$. For the base flow, electrical boundary conditions are insulating, $-\mathbf{n} \cdot \nabla \Phi = 0$, at all boundaries apart from the electrodes; at the inner electrode, a radial current is forced, $-\nabla \Phi = \mathbf{e}_r$, the outer electrode is set to ground, $\Phi = 0$ (Paper 1, Appendix A). For the linearized perturbation equations, the boundary conditions are the same as for the base flow apart from the electrical boundary condition for the inner electrode which is also insulating.

In order to have a perturbation in the linearized equations to begin with (which also satisfies the continuity equation), a flow is driven by the injection of a radial electrical current at the inner electrode which is shut off after some time. For our study, we applied $-\nabla \Phi = f(t)\mathbf{e}_r$ with

$$f(t) = \begin{cases} \frac{c}{2} (1 + \cos(\pi t/t_0)) & \text{for } t < t_0 \\ 0 & \text{for } t \geq t_0, \end{cases} \quad (10)$$

which is smooth at t_0 for which we used $t_0 = 0.1$. The constant c is adjusted in the range from 10 for $M = 10$

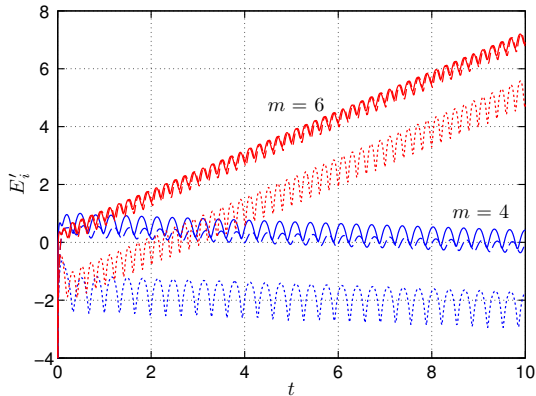


FIG. 2. Temporal evolution of nondimensional kinetic energies of perturbation E'_i where $i \in \{r, \phi, z\}$. The data are taken from runs with $M = 100$, $I = 0.22$ A and $m = 4$ (blue) and $m = 6$ (red) respectively. Continuous lines are E'_ϕ , dashed lines E'_r , dotted lines E'_z .

to 0.5 for $M = 200$ such that the kinetic energy in the perturbation of the flow is small ($\sim 10^{-3}$) compared to the base flow.

In the linear instability study, first the base flow model at (M, Re) is run until it converges. Then the flow for every azimuthal wave number m is simulated separately. The number of degrees of freedom ranges from roughly $1.6 \cdot 10^5$ at $M = 10$ to $3.1 \cdot 10^5$ at $M = 200$. Calculations were performed on a single processor with every run (M, Re, m) taking of the order of four hours of CPU time.

3. Parameters and processing

We perform a systematic parameter study of the first-order perturbation equations in order to calculate growth rates σ for the different modes and discover the threshold of linear stability. Moreover we study the spatial structure and behaviour of the unstable modes.

The parameter study of the base flow in Paper 1 contained models with $M \in [1...200]$. An asymptotic behaviour in terms of velocity scalings was found for $M \gtrsim 30$. In this parameter regime, the axisymmetric base flow ($m = 0$) is stable up to the highest forcing. We restrict our linear stability analysis to Hartmann numbers $M \in [10, 200]$. The imposed electrical current I , which defines the input Re in the numerical study, is chosen between 1 mA and 4.3 A. For 48 parameter combinations (M, I) , we run models with azimuthal wave number $m \in [1...10]$. To check the behaviour of the growth rates at higher m , we perform simulations with m up to 50 for the case $(M = 20, I = 0.43$ A). We measure the temporal evolution of the spatial components of the kinetic

energy of the perturbation,

$$E'_i = 0.5 \int u_i'^2 dS, \quad (11)$$

where $i \in \{r, \phi, z\}$ denotes the radial, azimuthal or axial component.

Figure 2 shows the temporal evolution of the kinetic energies for $M = 100$, $I = 0.22$ A, $m = 4$ and 6. After the shutdown of the initial excitation, the kinetic energies in the 2D section are oscillating around a curve of exponential decay ($m = 4$) or growth ($m = 6$). We fit an exponential function $Ae^{\sigma t}$ to the azimuthal kinetic energy of perturbation E'_ϕ using linear regression. Extracting σ from E'_r or E'_z yields the same result. Positive growth rates $\sigma > 0$ mean that infinitesimal perturbations grow and the flow is unstable. Since the frequency of the instability is experimentally observable, we also measure the oscillation frequency $2f$ of the azimuthal kinetic energy which is two times the frequency f with which the azimuthal velocity u'_ϕ oscillates. This is done using the Lomb-Scargle periodogram [27] due to the uneven sampling of the data in time (adaptive time stepping). The oscillation frequencies of radial and axial velocity components are the same as the azimuthal one.

B. Laboratory experiment

In the ZUCCHINI experiment, we study the instabilities of electrically-driven MHD flow, especially the ones occurring in the free Shercliff layer at the inner electrode. We also find indications for instability in the Hartmann layer.

1. Setup

The experimental setup consists of three main parts: the tank filled with liquid GaInSn in the form of a modified cylindrical annulus, coils that create the imposed magnetic field \mathbf{B} , and power supplies generating the current I (Fig. 1). The setup is described in detail in Paper 1. The tank is equipped with ultrasonic Doppler velocimetry (UDV) and potential difference probes (PDP) to diagnose the flow. The working fluid is MCP 11 alloy from 5N Plus UK Ltd. consisting of 65.9% gallium, 20.8% indium and 13.3% tin. It is liquid at room temperature; its relevant physical properties are given in Table I. Since it is easily oxidized, we keep the whole system under an argon overpressure of 0.2 bar at all times.

The data of this work come from two different realizations of this setup. The first one is the ‘Caylar’ setup which consists of three resistive magnetic coils in a modified Helmholtz arrangement reaching a maximum field strength of $B = 0.1$ T. The three SM 18-50 power supplies from Delta Elektronika provide a total forcing current up to $I = 150$ A. In the second setup, called ‘Cryo’,

TABLE I. Physical properties of GaInSn from Morley *et al.* [28]. The presented data resemble the MCP11 alloy from 5N Plus.

kinematic viscosity ν	$2.98 \cdot 10^{-7} \text{ m}^2/\text{s}$
electrical conductivity σ_e	$3.1 \cdot 10^6 (\Omega\text{m})^{-1}$
density ρ	$6360 \text{ kg}/\text{m}^3$
melting point T_m	10.5°C
sound speed c	$2730 \text{ m}/\text{s}$

a single thick superconducting coil set from Cryomag- netics, Inc. provides a magnetic field up to $B_{max} = 1 \text{ T}$. The electrical current between the electrodes is driven by six SM 18-50 power supplies and reaches a total forcing current of $I_{max} = 300 \text{ A}$. More detailed information on magnetic field geometry, current distribution and GaInSn handling is given in Paper 1.

2. Measurements

The flow in ZUCCHINI is measured by UDV and PDP. Since the two methods rely on different physical principles, they provide independent measurements allowing to mutually check the results. In the following section, we describe the measurement methods, the data processing, and present a data example.

We use the UDV system DOP3010 from Signal Processing S.A. with three multiplexed channels connected [29]. The UDV probes have an emission frequency of $f_e = 8 \text{ MHz}$. UDV is based on measuring shifts in the position of particles, in our case oxides of Ga, suspended in the fluid between two consecutive ultrasonic pulses. It gives a profile of the velocity component along the ultrasonic beam. For technical details and procedures, see Paper 1.

Two of the three UDV probes are mounted in the inner cylinder of the tank as shown in Figure 3. Probe R measures the radial velocity u_r along a radial profile to the outer wall. Probe X records the chordwise velocity u_χ which contains u_ϕ as well as u_r . UDV probe Z is mounted flush in the bottom plate of the tank slightly outside the inner disk electrode. It records a profile of the axial velocity u_z over the entire height of the container.

PDP measurements have not been used in Paper 1. Hence we give here a more detailed overview of the method. We employ PDPs which make use of the externally imposed magnetic field. The PDP measures the voltage drop $\Delta\Phi$ across the distance between the wires Δl induced by the flow of an electrically conducting fluid in a magnetic field. In the absence of electric currents \mathbf{j} , Ohm's law (Eq. 4) relates the electric field $E \approx \Delta\Phi/\Delta l$ linearly to the velocity [30]. In specific cases, it is necessary to take thermoelectric effects into account due to the different materials of PDP and fluid when measuring $\Delta\Phi$ [31, 32]. Also it is known that PDPs perturb liquid metal flow [33]. We consider these effects to be negligible

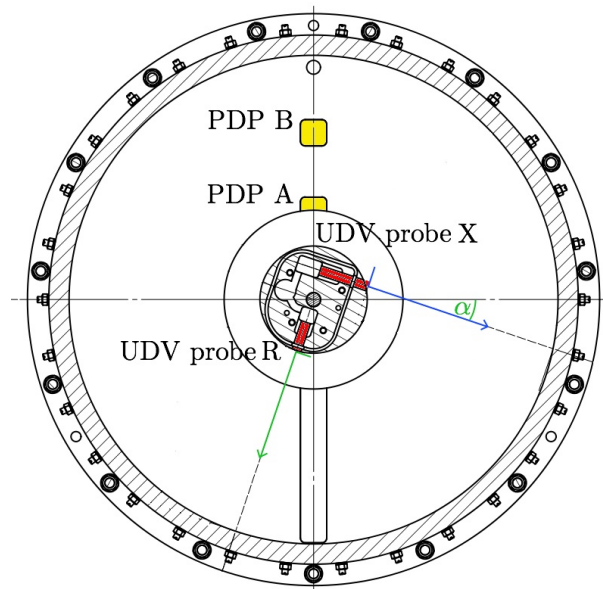


FIG. 3. Top view of tank with orientation of UDV probes R (radial) and X (chordwise) in red and the location of the potential difference probes A and B in yellow.

in our experiment.

We use an array of wires mounted flush in the top lid of the container to measure $\Delta\Phi$ in the r - and ϕ -directions in a similar way to that of Kljugin and Thess [34] and Messadek and Moreau [9]. Our PDP arrays consist of squares of 2×2 brass pins with a width of a few tenths of a mm and a spacing of 10.16 mm, thus yielding two radial and two azimuthal measurements per PDP array. The PDP arrays A and B are located on a radial ray above the radial UDV beam at $r = 75 \text{ mm}$ and 140 mm respectively. Since $\mathbf{B} \approx B_0 \mathbf{e}_z$, azimuthal and radial velocity are given by

$$u_{\{\phi,r\}} = \frac{\Delta\Phi_{\{r,\phi\}}}{B_0 \Delta l}. \quad (12)$$

In the limit of high Hartmann numbers, $M \gg 1$, the electric potential is uniform along the direction of the magnetic field and does not significantly change over the Hartmann layer. Hence our measurements of $\Delta\Phi$ in the Hartmann layer do not only give local velocities but carry information about the core velocity. We have verified that the velocities calculated from PDPs agree qualitatively with the ones measured by UDV. Nevertheless we report PDP measurements as voltages only in this study.

The PDPs are connected to a NI PXI-2501 multiplexer and a NI PXI-4070 data acquisition system through a LAN cable of category 5e or similar shielded cables. In the 0.1 V (resp. 1 V) range, the measurements have a resolution of 0.1 μV (resp. 1 μV). Sampling with roughly 50 Hz (resp. 750 Hz) leads to a noise level of less than $\sim 1 \mu\text{V}$ (resp. $\sim 10 \mu\text{V}$). Potential differences are measured against the inner electrode as common reference, and later combined to yield local measurements.

UDV and PDP provide time series of velocity and potential, respectively. The sampling rate of the UDV is adjusted according to signal quality and the ability to resolve the observed oscillations. In general it increases from ~ 1 Hz at low currents (steady flow) to ~ 30 Hz at 150-300 A. The recording time is set such that the frequency resolution is sufficient (~ 0.01 Hz). In general it decreases from ~ 150 s to ~ 60 s with increasing current. The sampling rate of the PDPs is 5.2 Hz per channel for low forcing currents and 83.3 Hz for high currents.

3. Processing

UDV and PDP time series are treated similarly. In both cases, we calculate the temporal mean value $\langle \cdot \rangle$ and the standard deviation σ_u . After detrending with a linear function and applying a Hann window to the time series, we perform a fast Fourier transform (FFT) to find the two dominant frequency components f_i and their respective amplitudes A_i with $i \in \{1, 2\}$. Only spectral peaks with $A_i > 10 \langle A \rangle$ are considered as significant frequency components where $\langle A \rangle$ is the average value of the radially stacked amplitudes.

PDP measurements are processed in a similar way. In general, they confirm the results from the UDV recordings. Hence we focus on the UDV data in this work. A PDP data example is given in Appendix B.

Profiles of mean azimuthal velocity $\overline{u_\phi}(r)$ are derived as

$$\overline{u_\phi}(r) = \frac{r}{e} \overline{u_\chi}(r), \quad (13)$$

where $e = 25$ mm is the distance of the UDV chord (probe X) to the origin. For a discussion on the reconstruction of u_ϕ , see Section V B in Paper 1. We define the spatial averaging along a profile in a cylindrical coordinate system as

$$\langle \cdot \rangle = \frac{\int \cdot r dr}{\int r dr}. \quad (14)$$

The radial range of averaging in the case of $\langle \overline{u_\phi} \rangle$ is $r \in [100, 150]$ mm. The Reynolds number is defined as

$$Re = \frac{\langle \overline{u_\phi} \rangle a}{\nu} \quad (15)$$

where $\langle \overline{u_\phi} \rangle$ is averaged both in time and space.

III. RESULTS

In this section, we present the results of the numerical and experimental investigations which do not overlap in parameter space but give complementary insights into the system. The first part is dedicated to the mean (time-averaged) flow which has been studied in terms of the base flow in Paper 1 for the cases with low forcing up to

$I = 9$ A only. Then we study the instability of the free shear layer as well as its structure and the shear layer width. The section is concluded by the friction factor which shows indication of a turbulent Hartmann layer at medium M and large forcing.

A. Mean flow

The mean flow $\overline{\mathbf{u}}$ is the basis on which possible instabilities develop. In Paper 1, we have shown that $\overline{\mathbf{u}}$ is dominated by its azimuthal component $\overline{u_\phi}$ due to the Lorentz forcing in our model. At large M and low forcing I , the numerical results of the base flow followed well the theoretical expression

$$u_\phi^{\text{BH}}(r) = \frac{I}{4\pi r \sqrt{\sigma_e \rho \nu}} \quad (16)$$

of Baylis and Hunt [6]. The experimental profiles in Paper 1 exhibited the same proportionality $\overline{u_\phi}(r) \sim I/r$, however, with 20% smaller absolute values.

Figure 4a shows profiles of the time-averaged azimuthal flow $\overline{u_\phi}(r)$ in the experiment at $M = 1769$ ($B = 875$ mT) for varying forcing current. The general shape of the profiles is similar as in Paper 1 up to the highest forcing of $I = 300$ A: a shear layer forms on the cylinder tangent to the inner electrode, separating the flow into an electrically forced outer domain and an inner domain where the flow is only viscously entrained from the forced region. This momentum diffusion appears to be enhanced at large forcing, broadening the free shear layer which we will study in Section III C.

Figure 4b shows the average value $\langle \overline{u_\phi} \rangle$ of the mean azimuthal flow as a function of the current I and the Hartmann number M . For large $M \gtrsim 500$, we observe a collapse of all data onto a linear scaling $\langle \overline{u_\phi} \rangle \sim I$ with the current up to the largest forcing. At lower $M < 500$, we observe a transition in the base flow. A low-forcing regime follows the same linear trend as for the highest M . Above a critical value of the injected current the mean flow tends to be less energetic, the amplitude increasing less rapidly with the current. The smaller M , the sooner this transition occurs. Although we do not have evidence from the present data, it is not excluded that this change of behaviour continues at the largest M but for currents that are out of reach with our setup. In the range of parameters accessible with this experiment, it is not possible to differentiate between a second linear behaviour and another mathematical form, which may lead to saturation at larger I . We will come back to this transition when looking at the friction factor in Section III E, especially Figure 14.

B. Instability of the free shear layer

For our understanding of the general dynamics in the modified cylindrical annulus, it is important to determine

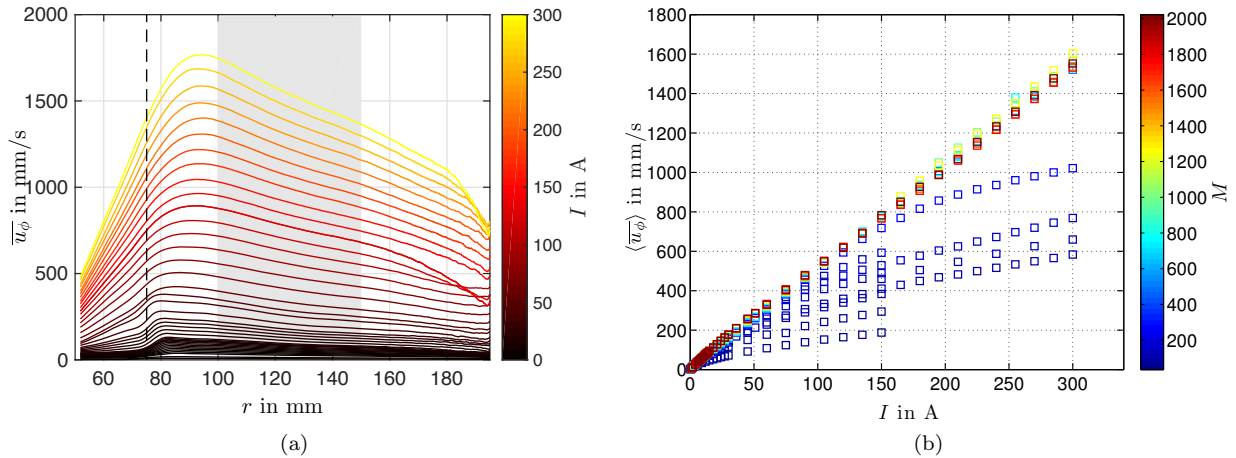


FIG. 4. (a) Profiles of mean azimuthal flow $\overline{u_\phi}(r)$ in the experiment at $M = 1769$ ($B = 875$ mT). The color indicates the forcing current I . The vertical line shows the location of the inner electrode, $r = 75$ mm; the grey window, $r \in [100, 150]$ mm, is used to calculate the average value $\langle \overline{u_\phi} \rangle$. (b) Radial average $\langle \overline{u_\phi} \rangle$ of the mean azimuthal flow in the experiment plotted versus forcing current I . The color indicates the Hartmann number M .

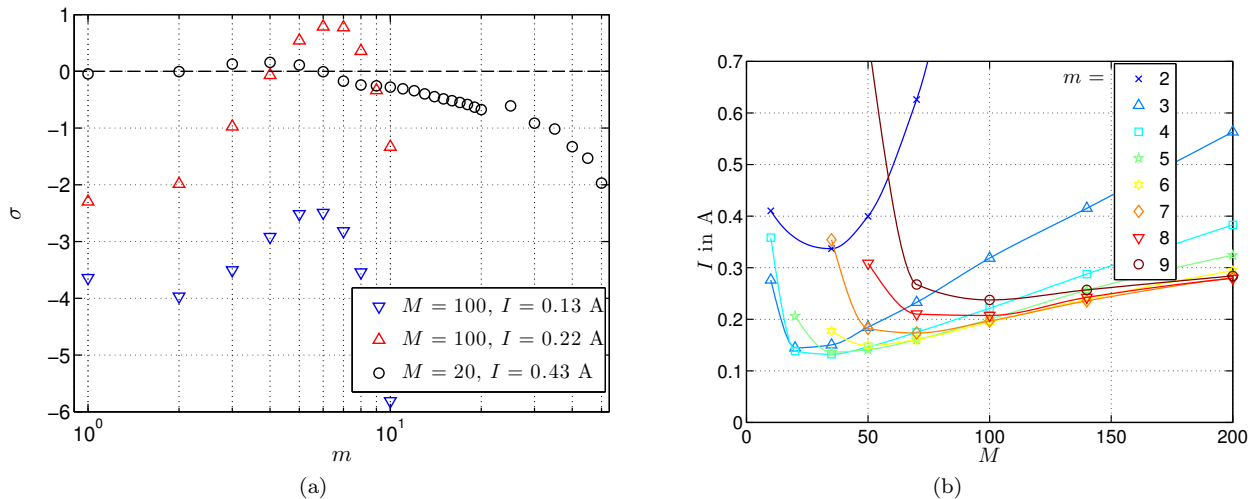


FIG. 5. Numerical linear stability study. (a) Growth rates σ versus azimuthal wave number m of the modes for ($M = 100, I = 0.13$ A and 0.22 A) as well as ($M = 20, I = 0.43$ A). Modes with $\sigma > 0$ are linearly unstable. (b) Curves of neutral stability ($\sigma = 0$) for different azimuthal wave numbers m in parameter space (M, I). The data points are derived from the measured growth rates by linear interpolation, the connecting lines are piecewise cubic Hermite interpolating polynomials.

the onset of the first instabilities that develop on top of the stationary base flow. Experimentally, the instabilities are, however, only unambiguously observed when they reach a certain amplitude and become significant in terms of energy compared to the base flow. Hence we start our study of the instabilities in the system by the numerical linear stability analysis described in Section II A.

Figure 5a displays the growth rate σ of modes with different azimuthal wave numbers m for three selected cases (M, I). At $M = 100$, all modes are stable for $I = 0.13$ A. For $I = 0.22$ A, the modes with $m \in \{5, 6, 7, 8\}$ are unstable whereas larger m are stable again. As seen in the case ($M = 20, I = 0.43$ A), the growth rate σ

decreases almost monotonically towards large m . In a 3D setup with all wave numbers present, all modes with $\sigma > 0$ might grow. After sufficient time, however, only the mode with largest σ is observed.

Through an interpolation, we find the critical current I_c for which $\sigma = 0$ at every (M, m). These curves of neutral stability are shown in Figure 5b. The lowest curve corresponds to the mode which becomes first unstable when increasing the current. The onset of linear instability is given by the lower envelope of all these curves. Its critical current I_c has a minimum of roughly 0.13 A at $M \approx 30$. For larger M , it increases to 0.28 A at $M = 200$; the scaling follows $I_c \sim M^{0.5}$. We observe that the wave

number m of the most unstable mode increases from 3 at $M = 10$ to 8 at $M = 200$. Since we are dealing with a linear stability study, we can not predict the wave number of the dominant mode for $I \gg I_c$. In the saturated regime, it is possible to find different modes, as we will see in the experimental data.

In the experimental UDV recordings, we use the standard deviation σ_{u_ϕ} of the azimuthal velocity as a tracer of the instability, i.e. the fluctuating part of u_ϕ . Figure 6a shows radial profiles of $\sigma_{u_\phi}/\langle\overline{u_\phi}\rangle$ at $M = 1769$ and varying current. Neglecting measurement noise, the quantity $\sigma_{u_\phi}/\langle\overline{u_\phi}\rangle$ can be interpreted as the square root of the ratio of energy in the instability to the energy in the base flow. We observe that $\sigma_{u_\phi}/\langle\overline{u_\phi}\rangle$ has a significant peak inside the edge of the inner electrode ($r = 75$ mm) already at the lowest forcing. This peak shifts to a slightly larger radius with higher forcing but stays near to the inner electrode. It indicates an instability localized at the free shear layer, which we will call regime 1 in Figure 6b. At this point, the instability is energetically not significant compared to the base flow.

At larger forcing current I , $\sigma_{u_\phi}/\langle\overline{u_\phi}\rangle$ increases while the peak broadens over a larger radial range. The instabilities grow in amplitude and are not restricted to the free shear layer anymore but become container-filling. We will call this regime 2 in Figure 6b, and take as a criterion for the transition that the radial average is $\langle\sigma_{u_\phi}\rangle/\langle\overline{u_\phi}\rangle > 0.1$ (dashed line). In regime 2, the instability alters the base flow as we will see when looking at the shear layer width in Section III C.

Figure 6c is a synopsis of the results from the numerical linear stability study and the transition between regimes 1 and 2 in the experimental data. This stability diagram in (M, Re) -space shows the linear onset Re_c as connected squares, experimental data points in regime 1 as open circles and the ones in regime 2 as filled diamonds.

All our experimental UDV measurements exhibit a localized peak of σ_{u_ϕ} at the location of the free shear layer. This result is well understood from the very threshold obtained in the numerical simulations. We tried to perform experiments at very low current to capture the onset of regime 1. However, the resolution of the UDV does not allow us to resolve both the large amplitude mean flow and the small amplitude fluctuations simultaneously.

The transition between regimes 1 and 2 in the UDV data is well described by $Re/M \approx 25$ for large M in Figure 6c. Hence we use this combined parameter to collapse the $\sigma_{u_\phi}/\langle\overline{u_\phi}\rangle$ data. Figure 6d displays $\langle\sigma_{u_\phi}\rangle/\langle\overline{u_\phi}\rangle$, where σ_{u_ϕ} was averaged over $r \in [60, 120]$ mm, versus Re/M for large $M \gtrsim 500$. The data appears to be well collapsed onto one curve that exhibits a clear transition, increasing by roughly an order of magnitude around $Re/M \approx 25$.

C. Shear layer width

As the instabilities appear to develop at the free shear layer for low forcing, it is instructive to have a closer look

at the properties of this layer. A measure that is accessible from profiles of azimuthal velocity $\overline{u_\phi}(r)$ (Fig. 4a) is the width δ_S of the free shear layer. We define it as the radial distance between the point of maximum azimuthal velocity and the edge of the inner electrode, $\delta_S = r(\overline{u_\phi}^{max}) - r_d$.

Figure 7a shows δ_S versus the current I for experimental runs at large $M \gtrsim 500$. The different- M data behave similarly with δ_S first dropping from 10 to 5 mm when increasing I , and then exhibiting two jumps to rather constant plateaus of 13 mm and 19 mm. Only the data points at 1 A do not follow this behaviour, and show a clear M -dependence with smaller δ_S at larger M .

Also the δ_S -data are collapsed onto a single line when using the parameter Re/M instead of I as seen in Figure 7b. The two transitions in δ_S from 5 mm to 13 mm and subsequently to 19 mm occur at roughly $Re/M \approx 25$ and 70, respectively. Hence the first increase in the shear layer width corresponds to the transition from regime 1 to 2. At the value of $Re/M \approx 25$, the instabilities start to fill the entire container as discussed in the previous section. This appears to enhance the radial transport of momentum and flatten the velocity gradient, thereby broadening δ_S .

D. Structure of the instability

After determining the threshold of the instability and its location, we turn to its structure. The numerical linear stability analysis allows to conveniently plot the perturbation velocity field \mathbf{u}' . Figure 8 displays four snapshots of \mathbf{u}' for the most unstable, slightly supercritical mode $m = 8$ at $M = 200$. The perturbation flow (as the base flow) is largely axially invariant due to the magnetic field. The radial and azimuthal velocity components, u'_r and u'_ϕ are of the same order and oscillate as seen in Figure 2. The four snapshots of Figure 8 are taken with equal time intervals over one period of oscillation. The perturbation flow corresponds to alternating vortices at the free shear layer that are swept with the mean flow.

The shear rate γ in the axisymmetric base flow is shown in Figure 9. It is defined as the magnitude $\gamma = |\boldsymbol{\gamma}|$ of the strain-rate tensor $\boldsymbol{\gamma} = (\nabla\mathbf{u} + (\nabla\mathbf{u})^T)$. By far the largest shear occurs in the Hartmann boundary layers at the top and bottom lids. But also the free shear layer at the edge of the inner electrode and the outer-wall boundary layer contain a significant amount of shearing. The first instabilities hence appear to be an instability of the free shear layer itself, similar to a Kelvin-Helmholtz instability.

When observing the vortices travelling with the mean flow from a fixed point in the laboratory frame, we measure the oscillation frequency f of the velocity components. Figure 10 shows f from the numerical study as a function of the current I for different M . For a given electrical current, frequencies are higher for larger M . Note that only perturbations above the threshold of in-

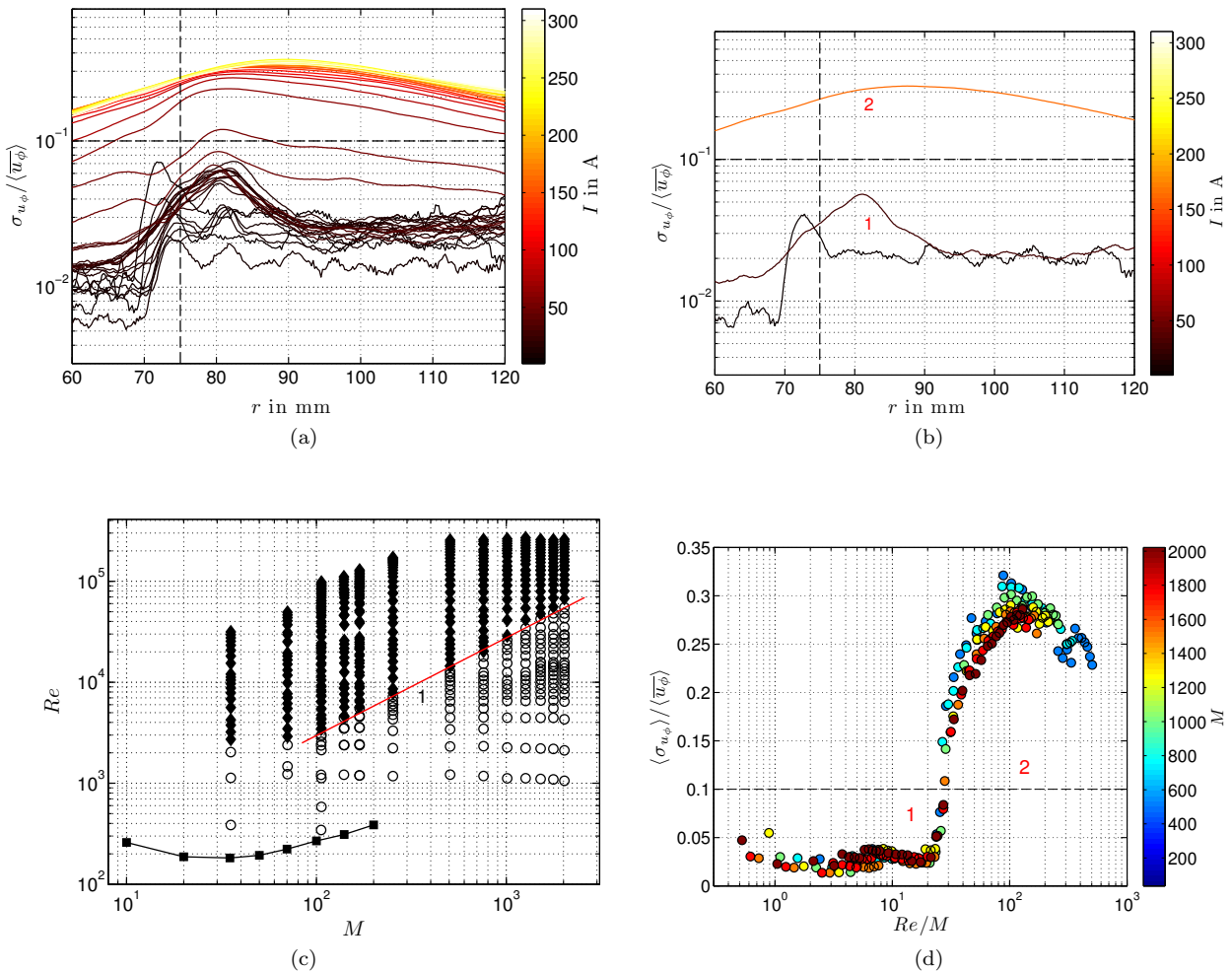


FIG. 6. Standard deviation and stability in the experimental data. (a) Profiles of the ratio of standard deviation σ_{u_ϕ} to mean azimuthal velocity $\langle \bar{u}_\phi \rangle$ at $M = 1769$ ($B = 875$ mT). The color indicates the electrical current I . The vertical line indicates the location of the inner electrode, $r = 75$ mm. (b) Example profiles from (a) showing (1) an instability localized at the free shear layer, and (2) a broad tank-filling instability with $\langle \sigma_{u_\phi} \rangle / \langle \bar{u}_\phi \rangle > 0.1$. (c) Measured data in (M, Re) -space with open circles corresponding to regime (1) and filled diamonds falling into regime (2). The red line with slope 1 appears to separate the two regimes well for $M \gtrsim 100$. The filled squares denote the critical Re for linear instability in the numerical study. (d) Averaged ratio $\langle \sigma_{u_\phi} \rangle / \langle \bar{u}_\phi \rangle$ for large $M \gtrsim 500$ versus Re/M showing a clear transition from regime (1) to (2) at $Re/M \approx 25$.

stability which is between 0.13 and 0.28 A depending on M (cf. Fig. 5b) are growing and potentially observable. Frequencies near the onset of linear instability range from roughly 4 mHz at $M = 10$ to 25 mHz at $M = 200$.

Oscillation frequencies in the experiment are determined by FFT from the UDV and PDP recordings as described in Section II B 3. Figure 11 displays the two dominant frequencies versus the current I for $M = 1769$. We observe a clustering of the frequencies on straight lines, f in general increasing with I . The largest dominant frequency observed at 300 A exceeds 7 Hz. UDV and PDP measurements both contain the same frequencies, and hence confirm each other. The various lines correspond to different modes present in the flow.

Adopting the picture of vortices being swept with the mean flow, we plot the dominant frequencies f versus

the radial average value of mean azimuthal velocity $\langle \bar{u}_\phi \rangle$ in Figure 12. Again we see a clustering of the data on straight lines through the origin which is the expected picture for the travelling Kelvin-Helmholtz instability. The wave number m of the instability is determined as

$$m = 2\pi r \frac{f}{u_t}. \quad (17)$$

Assuming the transit velocity u_t to be slightly above $\bar{u}_\phi^{max}/2$ as found by Messadek and Moreau [9] and $\bar{u}_\phi^{max} \approx 1.2 \langle \bar{u}_\phi \rangle$ in our data, we find $m = 2$ for the lowest mode. The second distinct line would correspond to $m = 6$, the steepest cluster at small velocities (small currents) to a mode with $m > 20$. Hence we observe a tendency towards larger-scale (low- m) structures with higher forcing. We propose that it can be interpreted as

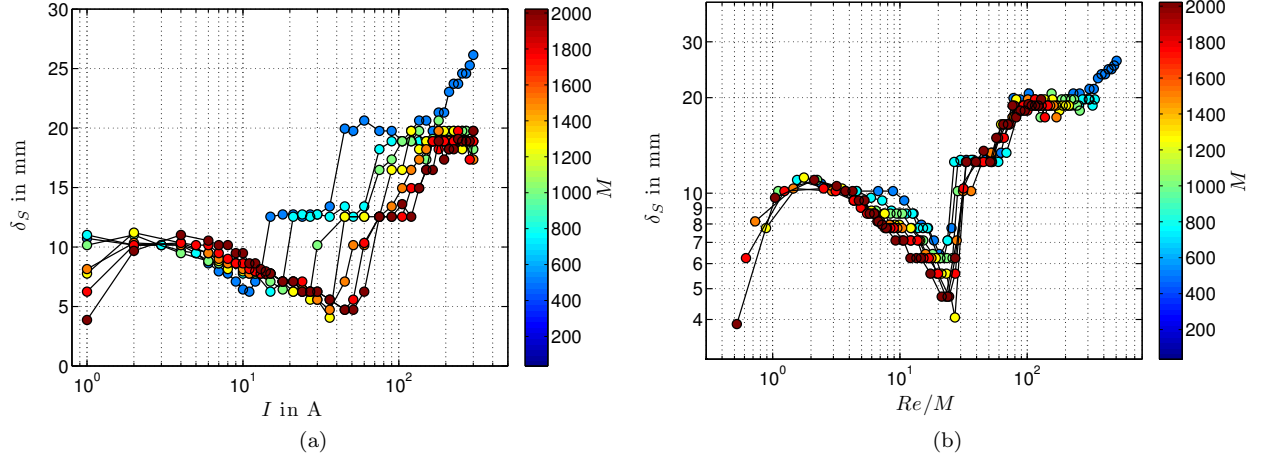


FIG. 7. Width δ_S of the free shear layer versus (a) the current I and (b) the parameter Re/M in large $M \gtrsim 500$ models; color indicates the Hartmann number M . We observe transitions in δ_S to 13 mm at $Re/M \approx 25$ and to 19 mm at $Re/M \approx 70$.

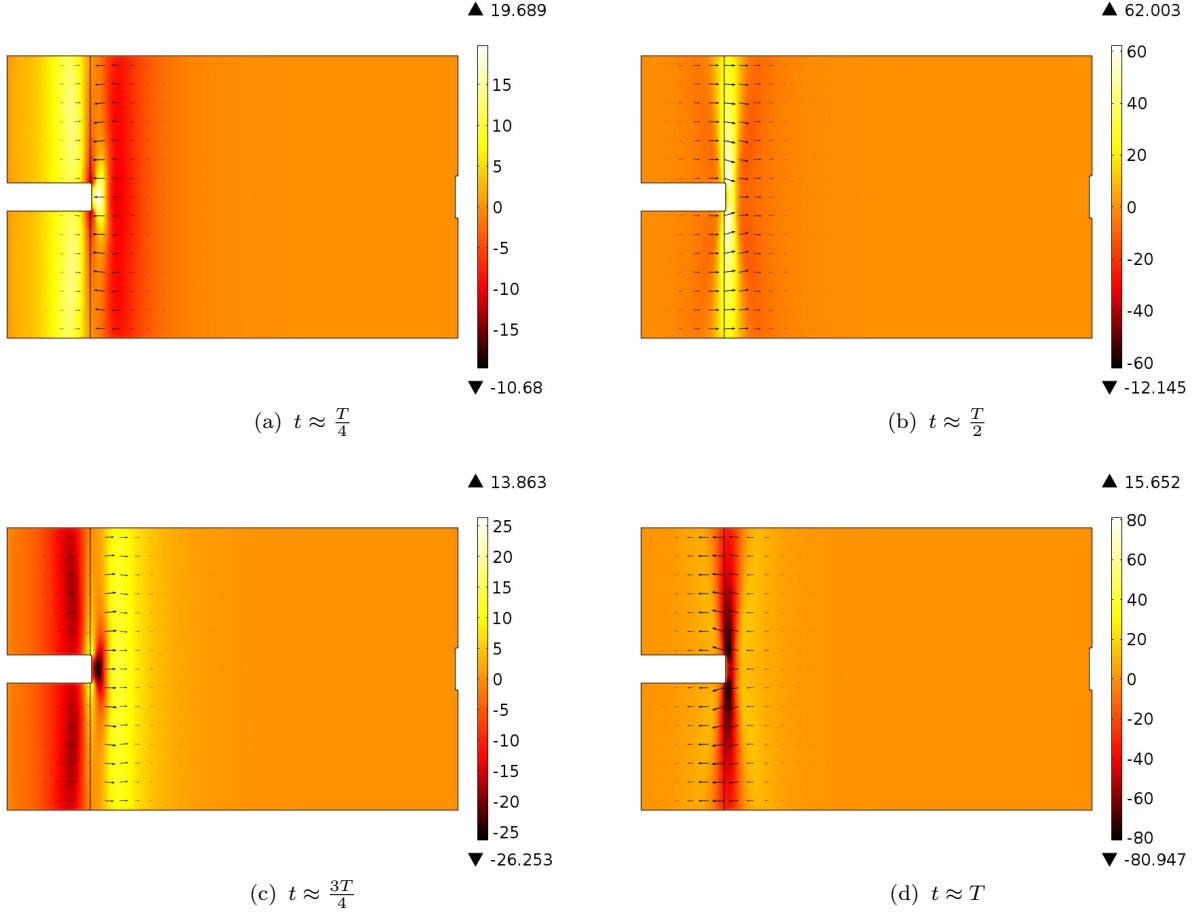


FIG. 8. Temporal evolution of the perturbation velocity \mathbf{u}' over one period for the slightly supercritical case ($M = 200, I = 0.34$ A, $m = 8$). Colours indicate the azimuthal velocity u'_ϕ , arrows show u'_r and u'_z . The four snapshots are taken with equal time intervals over one oscillation period T . Originating from the Shercliff layer at the inner electrode, the perturbation flow appears to meander with all velocity components changing sign over one period. The structure consists of alternating vortices being swept with the mean flow, and thus is attributed to a Kelvin-Helmholtz-type instability.

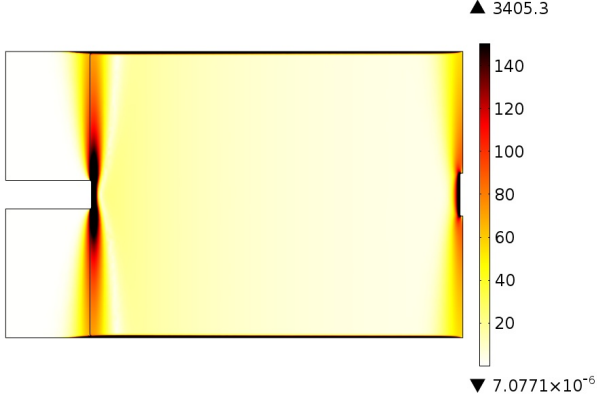


FIG. 9. Shear rate γ of the axisymmetric base flow for the slightly supercritical case ($M = 200, I = 0.34$ A, $m = 8$). Most shearing occurs in the very thin Hartmann layers at the top and bottom walls, followed by the free Shercliff layer at the inner disk electrode and the outer side layer. Note the cropped color scale.

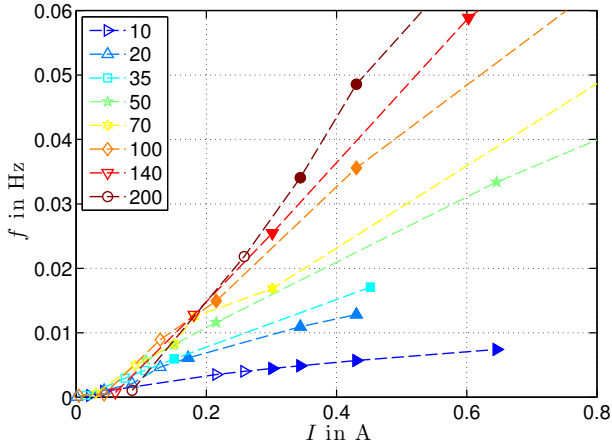


FIG. 10. Frequencies f of the oscillations of the azimuthal velocity u'_ϕ in the numerical linear stability study as a function of the forcing current. Colours indicate the value of the Hartmann number M ; note the different scale compared to the experimental data. Empty symbols denote decaying modes, filled symbols the fastest growing modes.

the inverse energy transfer leading to a merging of spatial structures in forced quasi-2D flows [8, 9].

In the numerical linear stability analysis, we found that the azimuthal wave number of the most unstable mode grows from $m = 3$ at $M = 10$ to $m = 8$ at $M = 200$ (Fig. 5). In the experiment, there appears to be a trend towards larger m (steeper lines) with increasing M at low forcing in agreement with the numerical prediction. The steepest cluster line which includes data with $M \gtrsim 500$ in Figure 12 corresponds to $m > 20$ in accordance with the extrapolation of the m present in the numerics. The decrease in m with Re as well as the increase with M are features also known from hydro- and magnetohydrodynamic spherical Couette flow [35, 36].

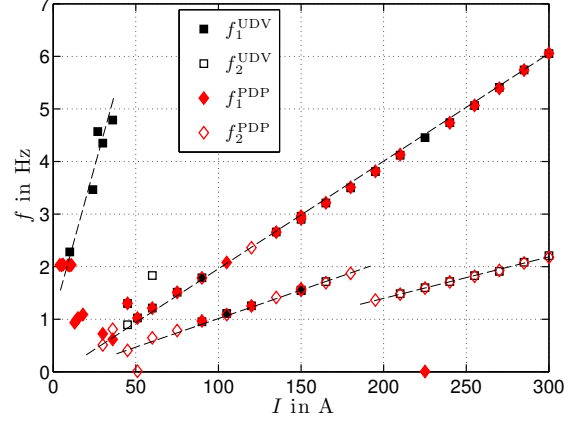


FIG. 11. Frequencies f_1 (filled) and f_2 (open) of significant spectral peaks from UDV measurements of u_χ (black squares) and PDP recordings of $\Delta\Phi_\phi^A$ (red diamonds). The selected data were taken at $M = 1769$ and have an energy larger than 10 times the noise level.

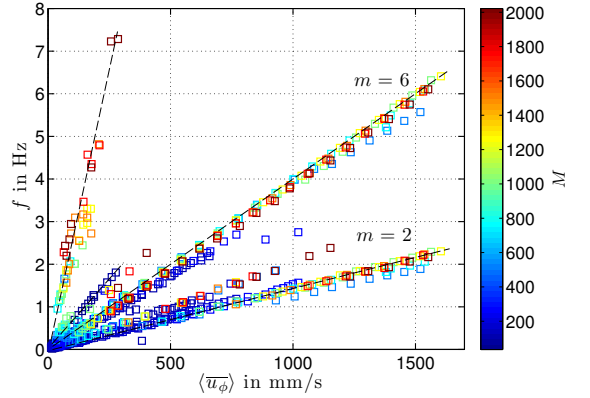


FIG. 12. Plot of dominant frequencies f_1 and f_2 in u_χ versus the radial average value of mean azimuthal velocity $\langle \bar{u}_\phi \rangle$. The data points cluster on straight lines through the origin. This suggests that the instabilities are traveling with the mean flow at a transit speed u_t . Under this assumption, the lowermost line corresponds to an azimuthal wave number of $m = 2$.

A difference between the linear stability analysis and the experiment is that in the first all values of m appear whereas the experiment is fully nonlinear and only a few distinct m are observed. A possible mechanism how this occurs was described by Kaplan [37]. Using nonlinear 3D simulations, the author revealed the energy pumping between modes with different m and formulated it as a network. This leads to saturation and to suppression of all modes but one. Experimentally, we hardly ever measure directly at the onset of instability and hence only observe the final saturated state.

We compare the wave numbers m found in the numerical analysis and the experiment with the prediction of a theoretical stability analysis for 2D instabilities in

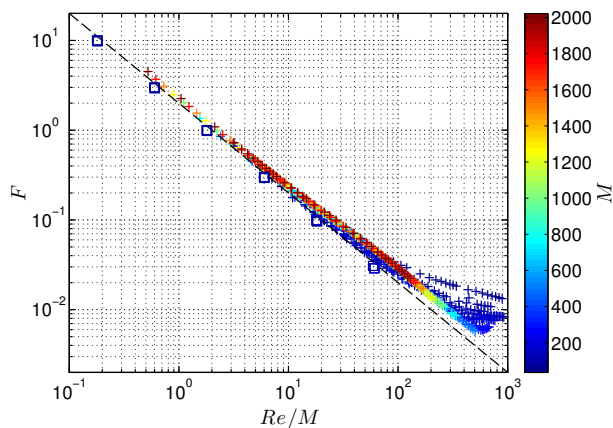


FIG. 13. Friction factor F versus Re/M as in [7]; colour indicates M . The crosses are the experimental data, the squares the numerical data from the base flow study with $M \in [50, 200]$. The dashed line gives the laminar value $F_{lam} = 2(Re/M)^{-1}$ from theory.

electrically-driven shear flow by Lieutaud and Neel [22]. At onset, similar wave numbers m as in our linear stability analysis are predicted, m increasing with M . Following [22], we would expect $m \approx 24$ for the onset of instability at $M = 2022$. Experimentally we observe wave numbers of this order at large M and low forcing.

E. Friction factor

The friction factor F quantifies the dissipation in the system. Hence it is well suited to study processes that significantly affect the total amount of dissipation. In their study of the stability of the Hartmann layer, Moresco and Alboussière [7] (hereafter referred to as MA04) used measurements of the friction factor and defined it as

$$F = \frac{IB}{u_m^2 \rho 2\pi r} \quad (18)$$

where the mean azimuthal velocity u_m was determined from measurements of the potential drop between inner and outer cylinder. We use $u_m = \langle \overline{u_\phi} \rangle$, the mean azimuthal velocity derived from UDV measurements. Figure 13 shows the relation between friction factor F and the parameter Re/M for our experimental and numerical data. As in MA04, the data with different M are pretty well collapsed in this plot. The dashed line shows the friction factor $F_{lam} = 2(Re/M)^{-1}$ for laminar flow. The numerical data from the base flow study obey F_{lam} well with the small difference coming from the definition of our local average. For the experimental data, we observe that the measured F follows F_{lam} up to $Re/M \approx 100$. For larger Re/M , the measured data transit to larger values of F . For lower M , this transition is gradual. For moderate M , the observed transition is more pronounced.

For a closer examination, Figure 14a shows the friction factor from the experimental data normalized by its laminar value, F/F_{lam} . Up to $Re/M \approx 4$, F does not exceed F_{lam} by more than 20%. For large M , we observe a gradual transition to $F/F_{lam} \approx 1.5$ at $Re/M \approx 70$. Above this value, depending on M , we observe a plateau followed by an abrupt increase of F/F_{lam} . This second transition is not well captured by a universal critical Re/M . In Figure 14b, the same quantity F/F_{lam} is plotted against Re/M^2 showing a clear transition around $Re/M^2 = \mathcal{O}(1)$ for all accessible M . This contrasts with earlier studies that found a transition in the Hartmann layer occurring at a critical $Re/M \approx 380$. The increase in F/F_{lam} above $Re/M^2 = \mathcal{O}(1)$ exhibits a power-law scaling of the form $F/F_{lam} \sim (Re/M^2)^\alpha$, with α increasing with M .

Due to its definition (Eq. 18), the friction factor F is linked to the average velocity $\langle \overline{u_\phi} \rangle$. Studying the friction factor in our case is equivalent to looking more closely at the behaviour of $\langle \overline{u_\phi} \rangle$ in Figure 4b. Figures 14c and d illustrate this correspondence.

IV. DISCUSSION AND CONCLUDING REMARKS

In this study, we report several transitions. The first one is well captured in our numerical linear stability analysis, and scales roughly as $Re \sim M^{1/2}$. In the accessible range of parameters of our experiment, we always operate in the unstable regime. The numerics suggest a Kelvin-Helmholtz-like instability mechanism emanating from the free shear layer.

At larger values of M and Re , unaccessible numerically, we observe further transitions. The first one occurring at $Re/M \approx 25$, which can be interpreted as a Reynolds number based on the thickness of the Hartmann layer, is associated with a significant increase in the amplitude of the fluctuating component (Fig. 6) and a pronounced change in the free shear layer thickness (Fig. 7b). Above this transition, the instability is no longer localized in the vicinity of the free shear layer but fills the entire fluid volume. These observations suggest a Hartmann layer destabilization mechanism. Furthermore, the critical value $Re/M \approx 25$ is consistent with the criterion for absolute stability derived by Lingwood and Alboussière [38] for an isolated Hartmann layer, $Re/M \approx 26$. In addition, the observed transition coincides with a mild increase in the friction factor deduced from the steady azimuthal velocity $\langle \overline{u_\phi} \rangle$ as seen in Figure 14a. The mechanism underlying the feedback effect of the fluctuating component onto the mean flow has yet to be established.

Yet another transition occurs at $Re/M^2 = \mathcal{O}(1)$, and is observed in the friction factor and the mean velocity (Figs. 14b and d). The transition is characterized by an abrupt increase in the dissipation, and thereby a decrease of $\langle \overline{u_\phi} \rangle$. Meanwhile, we do not see any significant

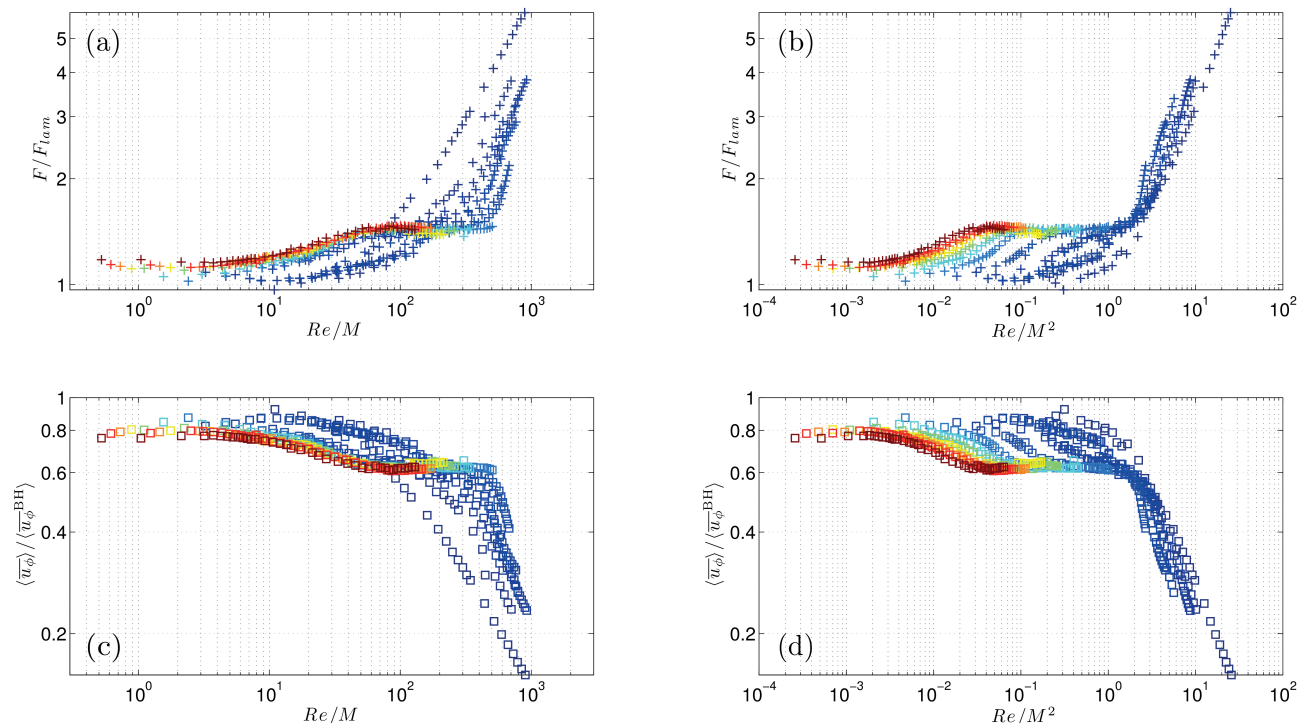


FIG. 14. First row: Friction factor F normalized by its laminar value F_{lam} . Second row: Average azimuthal velocity $\langle u_\phi \rangle$ normalized by its theoretical value $\langle u_\phi^{BH} \rangle$. Colors indicate M as in Figure 13. Plotting the data versus Re/M (a and c) collapses well the large- M runs in red and yellow, whereas the parameter Re/M^2 (b and d) appears to govern the significant transition at $Re/M^2 = \mathcal{O}(1)$.

changes in the frequency content at this parameter value (Fig. 12).

A similar sudden increase in F as at this third observed transition has been reported by MA04. In contrast with the present study, they proposed that the critical parameter governing their transition was $Re/M \approx 380$ rather than $Re/M^2 = \mathcal{O}(1)$. MA04 argued that the abrupt change in F results from the onset of turbulence in the Hartmann layer, which is commonly associated with a critical value of Re/M , the Reynolds number based on the Hartmann layer thickness.

It should be noted that there are three major differences between the MA04 experiment and the present one. First, their configuration did not give rise to a free shear layer. Second, the two experiments do not operate in the same parameter regime except for the cases $M = 169$ and 253. Although our setup can reach Hartmann numbers of order 2000, our limitations in injected electrical power do not allow us to achieve sufficiently high values of Re/M or Re/M^2 to observe this transition for $M > 253$. Third, the curvature ratio $\lambda = d/2r_m$ of channel half-width $d/2$ to mean radius r_m of the two experiments is very different. In the MA04 experiment, it was $\mathcal{O}(0.1)$, whereas it is $\mathcal{O}(1)$ in the present setup.

The last point has implications for the strength of the secondary (radial and axial) flow. Following Baylis and Hunt [6], secondary flows and associated inertial effects

are negligible in the large- M limit, if $(K/M^2)^2 \lambda \ll 1$, with the Dean number $K = \lambda^{1/2} Re$ measuring curvature effects. For $\lambda = \mathcal{O}(1)$ as in the present study, this criterion is equivalent to $N^2 \gg 1$ with the interaction parameter $N = (Re/M^2)^{-1}$. Hence the observed transition at $N = \mathcal{O}(1)$ can be interpreted as the point where inertial effects become negligible.

The MA04 experiment on the other hand operated in the inertialess regime even for $N \lesssim \mathcal{O}(1)$ due to the smaller curvature ratio. This could explain why they were able to observe transition to turbulence in the Hartmann layer with a scaling of $Re/M \approx 380$, while the present experiment detects a different transition, $Re/M^2 = \mathcal{O}(1)$, in the range of moderate Hartmann numbers, $M \lesssim 250$. Further investigations at higher current will be necessary to test whether the criterion for transition to turbulence in the Hartmann layer is also observed in our setup at asymptotically large M .

In conclusion, the ZUCCHINI study has been able to characterize different regimes of confined low- Rm MHD flow with increasing forcing: stable flow, an unstable free shear layer, unstable core flow and an unstable Hartmann layer. The numerical linear stability analysis and the experimental measurements with UDV and PDP provide complementary information, and yield a consistent picture of the dynamics.

For the future, it would be interesting to study how the flow in our modified cylindrical annulus is affected by a global rotation of the tank introducing a strong Coriolis force. Also it would be instructive to perform similar experiments with transparent electrolytes facilitating flow visualization. We are looking forward to seeing how the experience from ZUCCHINI is applied to study the magnetostrophic regime, i.e. a balance between Lorentz and Coriolis forces, in the rapidly-rotating spherical SpiNaCH (Spinning Sodium in Confoederatio Helvetica) experiment proposed by [39] which uses a

similar electrical driving for a flow of liquid sodium.

Appendix A: First-order perturbation equations in cylindrical coordinates

We give here the first-order perturbation equations in cylindrical coordinates for the numerical study of the linear onset of instability. Quantities describing the base flow are written with a superscript b , first-order perturbations are denoted by a prime.

$$\begin{aligned} & \frac{Re}{M^2} \left[\frac{\partial u'_r}{\partial t} + u'_r \frac{\partial u_r^b}{\partial r} + u_r^b \frac{\partial u'_r}{\partial r} + u'_z \frac{\partial u_r^b}{\partial z} + u_z^b \frac{\partial u'_r}{\partial z} - 2 \frac{u_\phi^b u'_\phi}{r} + \frac{u_\phi^b}{r} i m u'_r \right] \\ &= - \frac{\partial p'}{\partial r} + \frac{1}{M^2} \left[\frac{\partial^2 u'_r}{\partial r^2} + \frac{1}{r} \frac{\partial u'_r}{\partial r} - \frac{m^2}{r^2} u'_r + \frac{\partial^2 u'_r}{\partial z^2} - \frac{u'_r}{r^2} - \frac{2}{r^2} i m u'_\phi \right] \\ &+ B_\phi \frac{\partial \Phi'}{\partial z} - \frac{B_z}{r} i m \Phi' + u'_r (B_r^2 - 1) + B_r (u'_\phi B_\phi + u'_z B_z) \end{aligned} \quad (A1)$$

$$\begin{aligned} & \frac{Re}{M^2} \left[\frac{\partial u'_\phi}{\partial t} + u'_r \frac{\partial u_\phi^b}{\partial r} + u_r^b \frac{\partial u'_\phi}{\partial r} + \frac{u_\phi^b}{r} i m u'_\phi + u'_z \frac{\partial u_\phi^b}{\partial z} + u_z^b \frac{\partial u'_\phi}{\partial z} + \frac{u'_r u_\phi^b}{r} + \frac{u_r^b u'_\phi}{r} \right] \\ &= - \frac{1}{r} i m p' + \frac{1}{M^2} \left[\frac{\partial^2 u'_\phi}{\partial r^2} + \frac{1}{r} \frac{\partial u'_\phi}{\partial r} - \frac{m^2}{r^2} u'_\phi + \frac{\partial^2 u'_\phi}{\partial z^2} - \frac{u'_\phi}{r^2} + \frac{2}{r^2} i m u'_r \right] \\ &+ B_z \frac{\partial \Phi'}{\partial r} - B_r \frac{\partial \Phi'}{\partial z} + u'_\phi (B_\phi^2 - 1) + B_\phi (u'_r B_r + u'_z B_z) \end{aligned} \quad (A2)$$

$$\begin{aligned} & \frac{Re}{M^2} \left[\frac{\partial u'_z}{\partial t} + u'_r \frac{\partial u_z^b}{\partial r} + u_r^b \frac{\partial u'_z}{\partial r} + \frac{u_\phi^b}{r} i m u'_z + u'_z \frac{\partial u_z^b}{\partial z} + u_z^b \frac{\partial u'_z}{\partial z} \right] \\ &= - \frac{\partial p'}{\partial z} + \frac{1}{M^2} \left[\frac{\partial^2 u'_z}{\partial r^2} + \frac{1}{r} \frac{\partial u'_z}{\partial r} - \frac{m^2}{r^2} u'_z + \frac{\partial^2 u'_z}{\partial z^2} \right] \\ &+ \frac{B_r}{r} i m \Phi' - B_\phi \frac{\partial \Phi'}{\partial r} + u'_z (B_z^2 - 1) + B_z (u'_r B_r + u'_\phi B_\phi) \end{aligned} \quad (A3)$$

$$\frac{u'_r}{r} + \frac{\partial u'_r}{\partial r} + \frac{1}{r} i m u'_\phi + \frac{\partial u'_z}{\partial z} = 0 \quad (A4)$$

$$\begin{aligned} & \frac{\partial^2 \Phi'}{\partial r^2} + \frac{1}{r} \frac{\partial \Phi'}{\partial r} - \frac{m^2}{r^2} \Phi' + \frac{\partial^2 \Phi'}{\partial z^2} \\ &= - \frac{B_z}{r} i m u'_r + B_\phi \frac{\partial u'_r}{\partial z} + \frac{B_z}{r} u'_\phi + B_z \frac{\partial u'_\phi}{\partial r} - B_r \frac{\partial u'_\phi}{\partial z} - \frac{B_\phi}{r} u'_z - B_\phi \frac{\partial u'_z}{\partial r} + \frac{B_r}{r} i m u'_z. \end{aligned} \quad (A5)$$

Appendix B: PDP data example

PDP measurements are processed in the same way as UDV recordings in Section II B 3. Figure 15 shows example recordings of the eight PDPs in inserts A and B at $M = 1769$ and $I = 150$ A; both inserts provide time series corresponding to radial and azimuthal flow. The largest potential differences are the ones measured at the

outer azimuthal PDPs, $\Delta \Phi_{r,1}^B$ and $\Delta \Phi_{r,2}^B$, because of the large u_ϕ at this location. As $\Delta \Phi_{r,1}^A$ and $\Delta \Phi_{r,2}^A$ which show the largest-amplitude oscillations, they record the same signal. Potential differences connected to radial flow, $\Delta \Phi_\phi$, are oscillating around zero. The PDP measurements confirm our findings from the UDV recordings as e.g. seen from the coinciding frequencies in Figure 10.

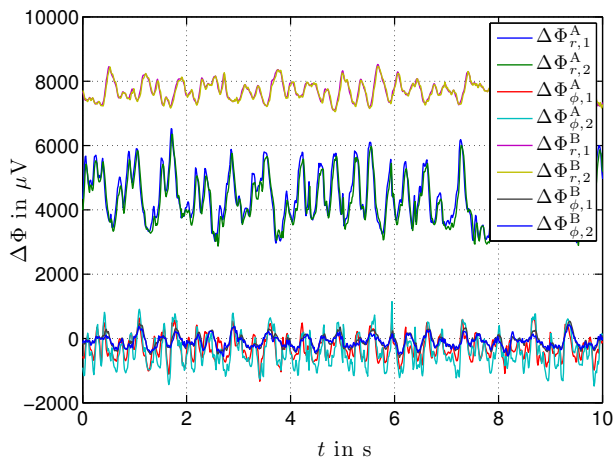


FIG. 15. Example time series of PDP: Potential differences $\Delta\Phi_r$ and $\Delta\Phi_\phi$ measured at the two inserts A and B indicating azimuthal and radial velocities, respectively, for $M = 1769$ and $I = 150$ A. Detail of the time series of all eight probes.

ACKNOWLEDGMENTS

We would like to thank P. Scarfe, R. Grimmer, F. Polli and T. Mörgele for help with the design and manufacture of the experiment as well as R. Hollerbach, T. Alboussière, A. Pothérat, F. Stefani, M. Seilmayer, T. Boeck and F. Samsami for fruitful discussions and advice on various topics within ZUCCHINI. The comments of two anonymous reviewers provided a missing link and helped improving the manuscript. Funding for this work from the ERC grant 247303 ‘MFECE’ and the SNF grant 200020_143596 is gratefully acknowledged.

-
- [1] P Olson, *Treatise on Geophysics*, edited by G Schubert, 8.01 Overview, Vol. 8 Core Dynamics (Elsevier, 2007) pp. 1–30.
- [2] PA Davidson, *An Introduction to Magnetohydrodynamics* (Cambridge University Press, 2001).
- [3] PA Davidson and F Siso-Nadal, “On the Structure of Small-Scale Motion in the Core of the Earth,” *Geophysical and Astrophysical Fluid Dynamics* **96**, 49–76 (2002).
- [4] Z Stelzer, D Cebon, S Miralles, S Vantighem, J Noir, P Scarfe, and A Jackson, “Experimental and numerical study of electrically-driven MHD flow in a modified cylindrical annulus: (1) Base flow,” *Physics of Fluids* (2015).
- [5] JA Baylis, “Detection of the onset of instability in a cylindrical magnetohydrodynamic flow,” *Nature* **204**, 563 (1964).
- [6] J Baylis and J Hunt, “MHD flow in an annular channel; theory and experiment,” *Journal of Fluid Mechanics* **48**, 423–428 (1971).
- [7] P Moresco and T Alboussière, “Experimental study of the instability of the Hartmann layer,” *J. Fluid Mech.* **504**, 167–181 (2004).
- [8] T Alboussière, V Uspenski, and R Moreau, “Quasi-2d MHD turbulent shear layers,” *Experimental Thermal and Fluid Science* **20**, 19–24 (1999).
- [9] K Messadek and R Moreau, “An experimental investigation of MHD quasi-two-dimensional turbulent shear flows,” *J. Fluid Mech.* **456**, 137–159 (2002).
- [10] J Boisson, A Klochko, F Daviaud, V Padilla, and S Aumaitre, “Travelling waves in a cylindrical magnetohydrodynamically forced flow,” *Phys Fluids* **24**, 044101 (2012).
- [11] J Hartmann and F Lazarus, “Hg-dynamics ii: Experimental investigations on the flow of mercury in a homogeneous magnetic field,” *Mathematisk-fysiske Meddelelser, Det Kgl. Danske Videnskabernes Selskab* **XV**, 1–45 (1937).
- [12] DS Krasnov, E Zienicke, O Zikanov, T Boeck, and A Thess, “Numerical study of the instability of the Hartmann layer,” *Journal of Fluid Mechanics* **504**, 183–211 (2004).
- [13] S Vantighem and B Knaepen, “Numerical simulation of magnetohydrodynamic flow in a toroidal duct of square cross-section,” *International Journal of Heat and Fluid Flow* **32**, 1120–1128 (2011).
- [14] Y Zhao and O Zikanov, “Instabilities and turbulence in magnetohydrodynamic flow in a toroidal duct prior to transition in hartmann layers,” *Journal of Fluid Mechanics* **692**, 288–316 (2012).
- [15] D Krasnov, O Zikanov, and T Boeck, “Numerical study of magnetohydrodynamic duct flow at high Reynolds and Hartmann numbers,” *Journal of Fluid Mechanics* **704**, 421–446 (2012).
- [16] D Krasnov, A Thess, T Boeck, Y Zhao, and O Zikanov, “Patterned Turbulence in Liquid Metal Flow: Computational Reconstruction of the Hartmann Experiment,” *Physical Review Letters* **110**, 084501 (2013).
- [17] A Pothérat, J Sommeria, and R Moreau, “An effective two-dimensional model for MHD flows with transverse magnetic field,” *Journal of Fluid Mechanics* **424**, 75–100 (2000).
- [18] A Pothérat, J Sommeria, and R Moreau, “Numerical simulations of an effective two-dimensional model for flows with a transverse magnetic field,” *Journal of Fluid Mechanics* **534**, 115–143 (2005).
- [19] T Alboussière, “A geostrophic-like model for large-Hartmann-number flows,” *Journal of Fluid Mechanics* **521**, 125–154 (2004).
- [20] T Alboussière, “Magnetohydrodynamics - historical evolution and trends,” (Springer, 2007) Chap. Geostrophic Versus MHD Models, pp. 195–209.
- [21] L Bühler, “Instabilities in quasi-two-dimensional magnetohydrodynamic flows,” *Journal of Fluid Mechanics* **326**, 125–150 (1996).
- [22] P Lieutaud and MC Neel, “Instabilities of an electrically driven shear flow,” *Comptes Rendus de l’Academie des*

- Science - Series IIB - Mechanics **329**, 881–887 (2001).
- [23] AH Roach, EJ Spence, C Gissing, EM Edlund, P Sloboda, J Goodman, and H Ji, “Observation of a Free-Shercliff-Layer Instability in Cylindrical Geometry,” *Physical Review Letters* **108**, 154502 (2012).
- [24] EJ Spence, AH Roach, EM Edlund, P Sloboda, and H Ji, “Free magnetohydrodynamic shear layers in the presence of rotation and magnetic fielda),” *Physics of Plasmas* **19**, 056502, 1–7 (2012).
- [25] HC Nataf, T Alboussière, D Brito, P Cardin, N Gagniere, D Jault, and D Schmitt, “Rapidly rotating spherical Couette flow in a dipolar magnetic field: An experimental study of the mean axisymmetric flow,” *Physics of the Earth and Planetary Interiors* **170**, 60–72 (2008).
- [26] D Schmitt, T Alboussière, D Brito, P Cardin, N Gagniere, D Jault, and H C Nataf, “Rotating spherical Couette flow in a dipolar magnetic field: experimental study of magneto-inertial waves,” *Journal of Fluid Mechanics* **604**, 175–197 (2008).
- [27] WH Press, SA Teukolsky, WT Vetterling, and BP Flannery, *Numerical Recipes*, 3rd ed. (Cambridge University Press, 2007).
- [28] NB Morley, J Burris, LC Cadwallader, and MD Nornberg, “GaInSn usage in the research laboratory,” *Review of Scientific Instruments* **79**, 056107, 1–3 (2008).
- [29] *DOP3000 series User’s manual*, Signal Processing S.A., www.signal-processing.com, software 4.01 ed.
- [30] S Eckert, A Cramer, and G Gerbeth, “Magnetohydrodynamics - historical evolution and trends,” (Springer, 2007) Chap. Velocity Measurement Techniques for Liquid Metal Flows, pp. 275–294.
- [31] L Davoust, M Cowley, R Moreau, and R Bolcato, “Buoyancy-driven convection with a uniform magnetic field. Part 2. Experimental investigation,” *Journal of Fluid Mechanics* **400**, 59–90 (1999).
- [32] B Sreenivasan and T Alboussière, “Experimental study of a vortex in a magnetic field,” *Journal of Fluid Mechanics* **464**, 287–309 (2002).
- [33] C Mistrangelo and L Bühler, “Perturbing effects of electric potential probes on MHD duct flows,” *Experiments in Fluids* **48**, 157–165 (2010).
- [34] A Kljugin and A Thess, “Direct measurement of the stream-function in a quasi-two-dimensional liquid metal flow,” *Experiments in Fluids* **25**, 298–304 (1998).
- [35] R Hollerbach, B Futterer, T More, and C Egbers, “Instabilities of the Stewartson layer Part 2. Supercritical mode transitions,” *Theoretical and Computational Fluid Dynamics* **18**, 197–204 (2004).
- [36] R Hollerbach, “Non-axisymmetric instabilities in magnetic spherical Couette flow,” *Proceedings of the Royal Society A: Mathematical, Physical and Engineering Sciences* **465**, 2003–2013 (2009).
- [37] EJ Kaplan, “On the saturation of non-axisymmetric instabilities of magnetized spherical Couette flow,” *Physical Review E* **89**, 063016, 1–8 (2014).
- [38] RJ Lingwood and T Alboussière, “On the stability of the Hartmann layer,” *Physics of Fluids* **11**, 2058–2068 (1999).
- [39] R Hollerbach, X Wei, J Noir, and A Jackson, “Electromagnetically driven zonal flows in a rapidly rotating spherical shell,” *Journal of Fluid Mechanics* **725**, 428–445 (2013).